



Automated Detection of Low-altitude Isolated Mesospheric Radar Echoes Using YOLOv8: Evidence for a C-Layer Phenomenon near 60 km Altitude?

Yadu Krishnan Krishnakumar^{1,3}, Toralf Renkwitz^{2,3}, and Andreas Ahrens³

¹Escuela Técnica Superior de Ingeniería y Sistemas de Telecomunicación (ETSIST), Universidad Politécnica de Madrid, Campus Sur, Calle Nikola Tesla s/n, 28031 Madrid, Spain

²Leibniz-Institute of Atmospheric Physics at the University of Rostock, Kühlungsborn, Germany

³Faculty of Engineering, Hochschule Wismar, University of Applied Sciences: Technology, Business and Design, 23966 Wismar, Germany

Correspondence: Yadu Krishnan Krishnakumar (yadu.krishnakumar@alumnos.upm.es)

Abstract. The Earth's ionosphere is created by the incident solar radiation and extends from approximately 60 km to 800 km altitude. Within the ionosphere distinct regions are formed based on the number density of the dominant chemical species and their ionization by the incident solar ultraviolet radiation and X-rays. The lowermost ionospheric region is called D region and expands during daytime downwards to approximately 60 km. In the recent years, rather faint echoes from below the typically continuous D region have been observed during the sunlit period using a 3.17 MHz ground-based radar system at polar latitudes. To our knowledge, this study might be the first evidence of such a phenomenon through consistent radar observations. Following an initial manual inspection of the raw data and the corresponding radar image spectra, an automated deep learning approach was employed to detect these isolated low-altitude echoes. We used the pattern recognition tool YOLO (You Only Look Once) to gain statistical information on the occurrence of these radar echoes over four years of radar measurements, which covered conditions ranging from minimum to maximum solar activity. The preferred altitude of these radar echoes is found to be near 58 km with typically little variability, and where the majority of detections show a rather narrow radar spectrum. Substantial annual variability was found for these parameters and the occurrence rate, essentially separating them into summer and winter. The reduced occurrence rates during the solar maximum year 2024 suggest the role of galactic cosmic rays as an ionisation source.

1 Introduction

With the presence of incident solar radiation, mainly ultraviolet and X-rays, the ionosphere is formed as atoms and molecules in the Earth's upper atmosphere are ionized. With the ionization of mostly nitrogen and oxygen free electrons are created that accumulate in certain ionospheric layers. These layers vary in intensity and peak heights with diurnal, annual and (multi-) decadal periodicities. The layers stretch from the D region at the bottom (~ 60-90 km) to the E region (~ 90-120 km) and on to the F region (~ 150-800 km). All of these regions and their variability play a significant role in radio wave propagation from very low frequencies like a few tens of kHz up to the microwave range of several GHz.

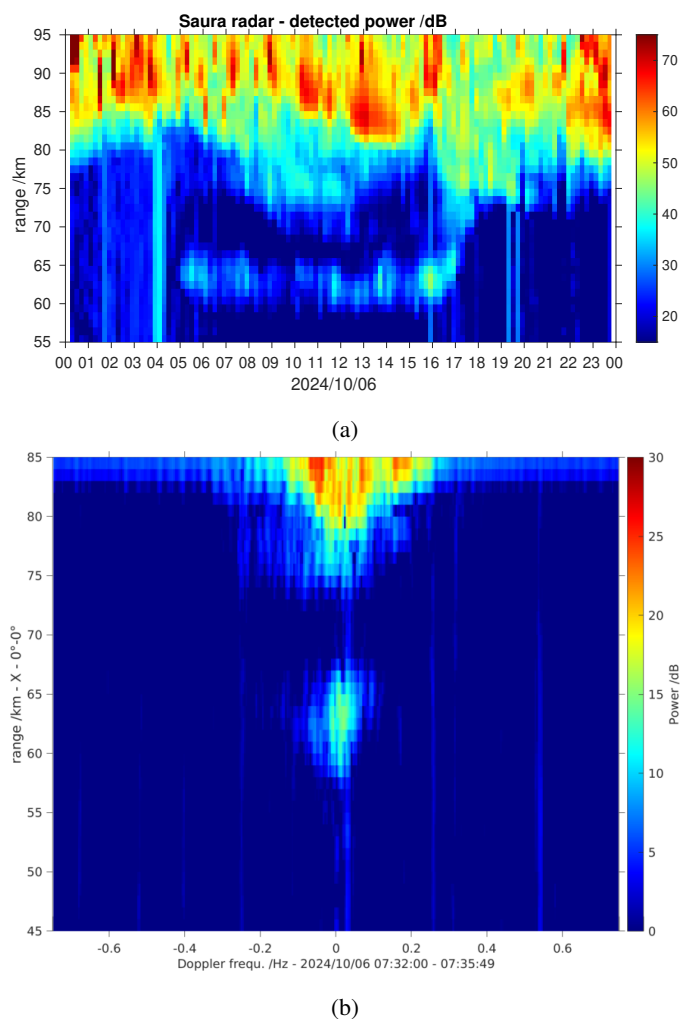


Figure 1. a) Detected power of the Saura radar for 6th Oct. 2024 showing an intense and long-lasting example of a low-altitude isolated mesospheric radar echo (LIME) at about 63 km altitude and the regular D region echoes above. b) Example of an image power spectrum of Saura for the same experiment and day as in Fig. 1a) showing regular D region echoes above 73 km and LIME near 63 km.

The upper regions (E and F) are monitored by various radar systems, but the most continuous and systematic approach is the Ionosonde HF sounder, probing the ionosphere since many decades with radar frequencies of typically 1 - 10 MHz (see e.g. Galkin et al., 2006). These systems are used to gain information about the actual condition of these regions and layers within, but also allow long-term analysis of its variability (see e.g. Sivakandan et al., 2025). The bottomside of the ionosphere is generally less well monitored because its density, and therefore the gradients are also much smaller, which limits the available measurement techniques. In situ measurements with sounding rocket payloads contributed significantly, but are limited in



temporal coverage (e.g. Friedrich et al., 2017). In the recent years, the monitoring of very low frequency transmissions (VLF) gained popularity to infer the D region situation (e.g. Siskind et al., 2018). Another option are medium or high frequency radar observations (see e.g. Reid, 2015), which can be used to measure the dynamics as well as the electron density within the D region (e.g. Renkwitz et al., 2018, 2023).

The general understanding is that the D region forms the bottomside of the ionosphere. Radar observations at the boundary of MF and HF range, however, showed the recurring presence of rather faint echoes that are well separated from the D region signals. Fig. 1a depicts one such intense event, showing a very persistent echoing layer at around 63 km that is clearly separated from the typical D region echoes. Radar echoes from near 60 km at polar latitudes occur actually quite frequently, but these are caused by the rapid increase of electron density due to energetic particle precipitation (EPP) (see e.g. Renkwitz and Latteck, 2017).

The radar echoes referred to in this manuscript are not related to EPP, as they exhibit distinctly different behaviour in the time series power spectra and continued visibility of the D region and the layers above. An example of corresponding power spectra of such an event is shown in Fig. 1b. The phenomenon appears to be connected to the incident solar radiation as it is almost exclusively seen during daytime and is also rather localized near 60 km altitude. To summarise these properties we will refer to them from now on as Low-altitude Isolated Mesospheric radar Echoes (LIME).

In this paper we describe an automated Deep Learning approach to identify LIME and by that having an efficient and robust way to derive statistics of their occurrences for four years of measurements (2018-2020, 2024). For that we apply a pattern recognition by a convolutional neural network based on radar image spectra to detect these isolated layers.

Object detection is a computer vision technique that identifies and spatially localises specific features within images. It provides an efficient framework for the automated detection of echoes in radar spectra. Unlike manual inspection, which is time-consuming and labour-intensive, deep learning-based object detection can systematically process large datasets while providing the precise spatial boundaries of detected echoes in altitude and frequency. In this paper, we utilise YOLO (You Only Look Once), a single stage object detection framework well known for its strong generalisation capability (Redmon et al., 2016). Specifically, we employ YOLOv8 (Ultralytics, 2023), which provides simultaneous classification and localisation, allowing for automated extraction of altitude and frequency parameters from detected echoes. This automated detection across multi-year datasets enables statistical analysis of the characteristics and occurrence patterns of LIME, which can provide insights into the underlying process.

The remainder of this paper is organised as follows. Section 2 describes the Saura radar system and observational dataset. Section 3 details the YOLOv8 object detection methodology, model training, and automated detection pipeline for parameter extraction. Section 4 presents results with model performance metrics and statistical analysis of detected echoes including altitude range, spectral extend, and temporal distributions. Section 5 discusses the seasonal variations, solar cycle dependencies, and detection methodology performance. Finally, some concluding remarks are provided in Section 6.



60 2 Instrumentation and data - the Saura radar

The observational data origins from the Saura radar located at 69.1°N and 16.0°E, which operates at a frequency of 3.17 MHz. Due to its relatively low frequency at the boundary of the medium and high frequency range it is capable to detect echoes from the bottom side of the ionosphere, namely the D region, which are caused by partial reflection at the vertical gradient of electron density. The system was built in 2002 and is since employed to monitor the dynamics in the mesosphere between typically 60
65 and 90 km altitude (see e.g. Singer et al., 2008). For most of the time distinct experiments are conducted to probe either only the vertical direction or scanning also to different oblique directions to e.g. measure radial velocity components in order to deduce horizontal and vertical velocities. For such measurements a sufficiently narrow beam width is mandatory, which is achieved by the antennas array of in total 31 antennas, of which 29 are arranged in a mills-cross configuration, spreading horizontally over nearly 1x1 km. Since the last upgrades the system is capable of coded signals, e.g. 4-bit-complementary codes are frequently
70 used to increase the average power and suppress interfering signals. Furthermore the receiver has 9 channels in total, which are connected to the entire main array of 28 antennas in order to form a narrow beam while the remaining 8 channels are connected to individual antennas for interferometric purpose. Further details on the radar and its measurement techniques are given in e.g. Renkwitz et al. (2018).

Here in this study, we only utilize the data from vertical beam pointing of the main array and the polarization of the ex-
75 traordinary magneto-ionic component. The data origins from one radar experiment that has been conducted sequentially in an unchanged configuration throughout the years. The maximum pulse-repetition frequency of the radar experiment was 100 Hz, which gives a range unambiguity of 1500 km.

The analysis described in the next section bases on the raw data time series acquired by the radar, from which image spectra are calculated and are then processed by YOLO. For this study, we initially have analyzed data covering the years 2018-2020 and
80 extended this with data from 2024 in order to also examine substantially different scenarios of very low and high solar activity. The ultimately analyzed data are image files in PNG format containing the image power spectra from the Saura radar. The spectra are calculated for each individual experiment runtime of 220 s for the radar ranges of 45 to 85 km. Additional coherent integrations are applied during daytime, but a total spectral coverage of 1.5 Hz is maintained, which is more than required for natural targets at these altitudes. To enhance consistent features in the image spectra and suppress outliers, a Savitzky-
85 Golay filter is applied for smoothing. In total 343196 image power spectra are analysed by YOLO to derive statistics of LIME detections.

3 Methodology

This study employs an object detection algorithm called YOLO to detect comparably faint low-altitude isolated mesospheric echoes that appear at approximately 60 km altitude in the lower mesosphere. The model developed using the YOLO algorithm
90 is utilised to derive the occurrence statistics of these echoes. In the following subsection, the justification for choosing YOLO over other methods, a brief high-level overview of the YOLO architecture, the complete implementation workflow, the man-



ual annotation process of the radar image spectra and the YOLO model training are explained. Finally, an assessment was conducted to evaluate the performance of the trained model.

3.1 YOLOv8 architecture and selection

95 We selected YOLO for this application due to its strong generalisation ability when applied to new domains (Redmon et al., 2016). Specifically we employed YOLOv8, an advanced modified version of YOLO developed by Ultralytics in 2023. It has proven good performance in various computer vision tasks like object detection (Al Mudawi et al., 2023), image classification (Oh and Lim, 2023), and instance segmentation (Sampurno et al., 2024). A recent comparative study conducted by Arabboev et al. (2024) demonstrates the superior performance of YOLOv8 over other object detection algorithms. In their study, YOLOv8
100 achieved a mean average precision index mAP50-95 of 37.1% and mAP50 of 52.1% on the COCO (Common Object in Context) dataset. One of the key advantage of YOLOv8 is its anchor-free detection approach. This eliminates the need for a template based predefined anchor boxes that were used in previous YOLO versions and several other detection methods. With this new architecture, the detection process is simplified by directly predicting the object corners and dimensions. Thus allowing the model to adapt to objects of varying shapes and sizes. This anchor-free detection approach is really helpful in the
105 detection of LIME as these echoes usually exhibit small variation in sizes and shape. This work utilised the smallest and the fastest YOLOv8n ('n' stands for nano) model for training. The implementation of YOLOv8 to remote sensing applications has been demonstrated by e.g. Ma et al. (2025) for their InSAR-YOLOv8 study and also provides a validation. According to their work the YOLOv8n base model achieved a very good detection accuracy of 96.76% mAP50 for landslide detection in InSAR measurements. Therefore, YOLOv8 should also provide good accuracy for the radar targets investigated in this study.

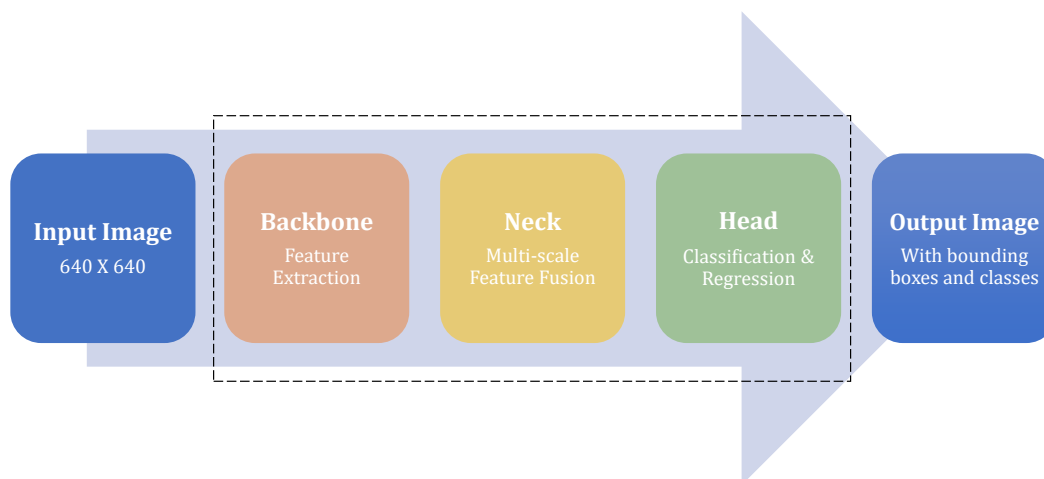


Figure 2. High-level overview of YOLOv8 architecture

110 Figure 2 illustrates the high-level overview of the YOLOv8 architecture, consisting mainly of 3 components: a backbone network for feature extraction, a neck component for feature fusion, and a head component for final predictions (Ma et al.,



2025). This streamlined architecture allows efficient single-shot object detection, completing the entire detection process in one forward pass. The Backbone helps in feature extraction. It has a series of convolutional layers organised into blocks that progressively downsample the input image while extracting increasingly complex features. Backbone produces feature maps at multiple scales, capturing both fine-grained details from early layers and high-level information from deeper layers. The Neck acts as a bridge between the backbone and the head. It implements feature fusion that combines information from different scales. It uses both top-down and bottom-up pathways to combine high-level features with low-level spatial details. This ensures that final feature representations contain both the high-level understanding needed for accurate classification and spatial precision required for precise localization. The Head represents the final prediction stage. It utilises two specialised networks, one focuses solely on identifying what type of object it found, while other focuses solely on determining the exact location. The entire architecture operates on the principle of single-pass detection. It processes the complete input image simultaneously rather than analyzing separate regions sequentially.

3.2 Implementation Workflow

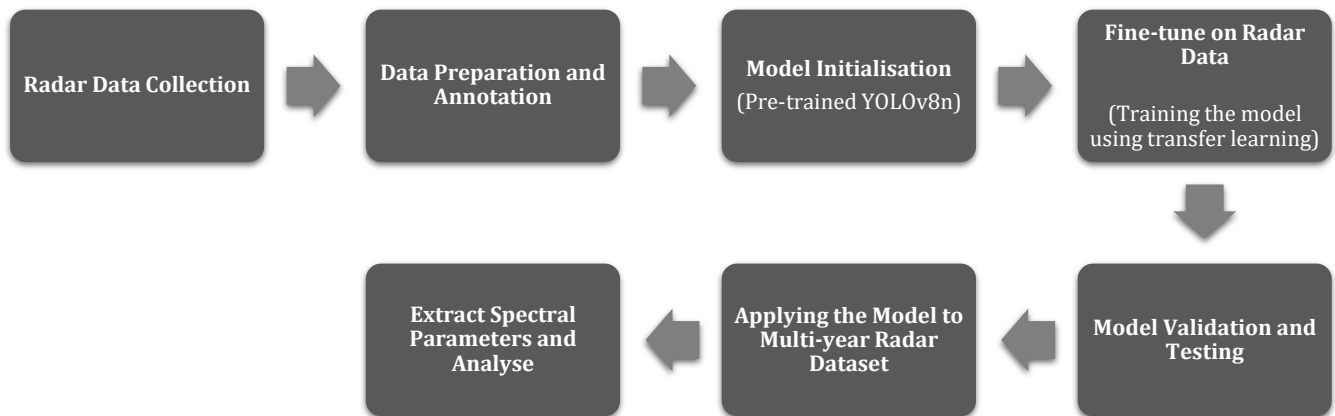


Figure 3. Implementation workflow for automated target signal detection

Figure 3 presents the detection methodology. The observational radar data were collected from the Saura radar (see Sect. 2.1). Each of these images in the dataset was annotated to label two different classes namely: 'Target_Signal' and 'Void'. Employing a transfer learning approach, the pre-trained YOLOv8n model was fine-tuned using the annotated radar spectra. Following that, the model was assessed using precision, recall, and mAP metrics. Once validated, the model was applied to detect LIME from the multi-year dataset. Detection's bounding box coordinates were converted to physical parameters. Each of these detections was then analysed to extract key parameters such as minimum altitude, maximum altitude, minimum frequency, and maximum frequency. Finally, these extracted data were analysed to understand the statistical behaviour of LIME.



3.3 Dataset preparation and annotation

For model training, testing, and validation, 200 images of radar spectra were selected based on manual inspection, prioritising clear examples of presence of distinct LIME. Each image in the dataset corresponds to one radar observation with a runtime of 220 s. Annotation tools were required to manually annotate these LIME signatures. For this purpose, we selected Roboflow (https://roboflow.com) as the annotation platform for its user-friendly web-based interface and seamless export to YOLOv8 format, after evaluating alternatives such as the Computer Vision Annotation Tool (CVAT). The annotation process focused on identifying the LIME occurring at approximately 60 km altitude while ensuring clear separation from other echoes. As

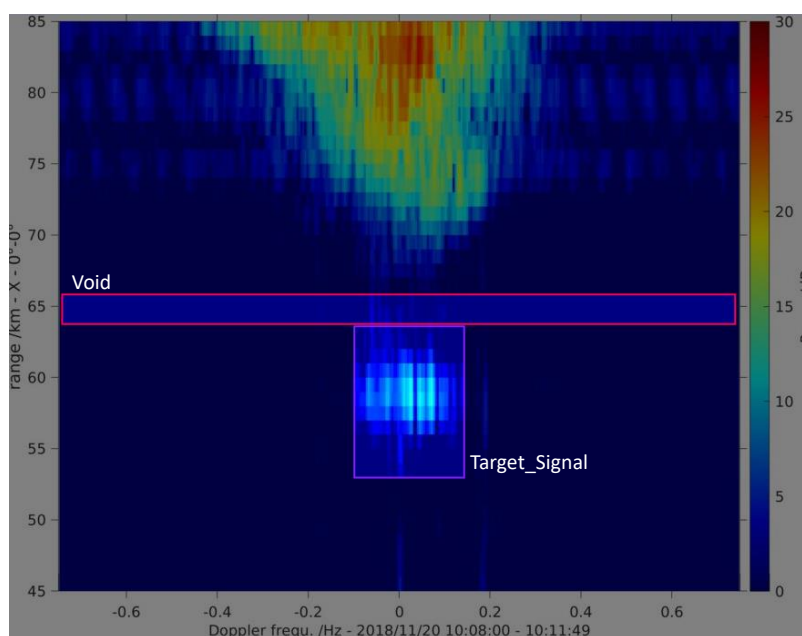


Figure 4. Example radar power spectrum showing annotated 'Target_Signal' and 'Void' classes used for YOLOv8 training.

illustrated in Fig. 4, for the annotation we employed a two-class system to address the specific challenge of correctly identifying LIME from the other echoes. LIME as defined earlier are isolated radar echoes appearing at an approximate altitude of 60 km with sufficient spatial separation from D region echoes that appear at higher altitudes. To ensure such spatial separation, area with no signal presence directly above LIME was annotated as "Void" class, while the LIME signatures were labeled as "Target_Signal" class. The final dataset consists of 200 radar spectra (PNG format). The dataset was further divided into 140 training images (70%), 40 validation images (20%), and 20 test images (10%). After the completion of annotation, the dataset was exported from Roboflow in YOLOv8 format.



145 3.4 Training configuration

In this work, we used Google Colab as the training environment. We employed transfer learning approach using a pre-trained YOLOv8n model, which was originally trained on the COCO (Common Objects in Context) dataset. The COCO dataset contains over 330,000 very diverse natural images with different shapes and sizes. These base models can be used as a starting point to adapt to a new task with limited datasets and less time (Ferguson et al., 2018). Pre-trained models have already
150 learned the ability to extract detailed features like edges, textures, and colors. This feature extraction capability often remains applicable to new domains (Situ et al., 2023). The YOLOv8n base model was then fine tuned by training it with the annotated radar spectra images for detecting LIME. This transfer learning approach eliminated the need to train the model from scratch and also allowed us to have a limited dataset of 200 annotated images. Data augmentation was applied using YOLOv8's default augmentation pipeline (Ultralytics, 2023). The model was trained for 50 epochs and validation was performed after each epoch to monitor model convergence. Table 1 summarises the key training configuration parameters used in this work:

Table 1. Training configuration parameters

Parameter	Value
Model Architecture	YOLOv8n
Pre-trained Weights	yolov8n.pt (COCO dataset)
Training Epochs	50
Batch Size	16
Optimizer	AdamW
Learning Rate	0.00167
Training Platform	Google Colab
Hardware	CPU (Intel Xeon 2.20GHz)
Training Duration	1.54 hours
Framework Version	Ultralytics 8.3.161
Software Environment	Python 3.11.13

155

3.5 Performance metrics

For the purpose of evaluating the model, we used the standard object detection evaluation metrics: precision, recall, mAP50, and F1. Precision and recall values are derived from confusion matrix elements such as true positives (TP) that represent correctly detected LIME signature, false positives (FP) indicating wrong detections, and false negatives (FN) which denote missed
160 LIME signatures. Precision measures the accuracy of positive predictions (see Eq. 1). Recall assesses detection completeness by determining the fraction of actual LIME successfully identified (see Eq. 2). The F1 score provides a balanced measure of a model's ability to accurately identify LIME combining both precision and recall (see Eq. 3). These evaluation metrics have been widely adopted for assessing deep learning models in computer vision applications (Dev et al., 2017; Guo et al., 2024).



Mean Average Precision (mAP) extends evaluation by integrating precision-recall performance across multiple confidence thresholds and intersection over union criteria (Ma et al., 2025). The mAP50 metric, which is calculated at IoU (Intersection over Union) threshold of 0.5, serves as the primary detection accuracy indicator.

$$\text{Precision} = \frac{\text{TP}}{\text{TP} + \text{FP}} \quad (1)$$

$$\text{Recall} = \frac{\text{TP}}{\text{TP} + \text{FN}} \quad (2)$$

$$\text{F1} = \frac{2 \times \text{Precision} \times \text{Recall}}{\text{Precision} + \text{Recall}} \quad (3)$$

3.6 Automated detection pipeline

Following the model evaluation, the trained model was applied to multi-year (2018-2020 and 2024) radar datasets to detect LIME and extract altitude and frequency parameters related to LIME. Each of these yearly datasets contains between 84,000 to 92,000 radar spectra images organised in monthly subfolders.

Each yearly dataset was processed sequentially. A crucial part of the detection process was the two-class validation approach for confirming LIME isolation. The algorithm extracted parameters from the identified LIME only when both 'Target_Signal' and 'Void' classes were detected, with 'Void' positioned above 'Target_Signal'. This ensured that the detected echo represented LIME with sufficient separation from D region echoes. It took approximately 3 hours to process each year.

After detection, the algorithm calculated four key parameters through pixel-to-physical unit conversion: minimum altitude, maximum altitude, minimum frequency, and maximum frequency. The minimum altitude represents the lower boundary of the bounding box, while the maximum altitude represents the upper boundary of the bounding box. Similarly, the minimum frequency corresponds to the left boundary and maximum frequency corresponds to the right boundary of the bounding box. The pixel-to-physical unit conversion factors were defined by identifying the pixel boundaries of the radar spectrum plotting area and their corresponding physical measurement values, as specified in Table 2.

Table 2. Pixel-to-physical unit conversion parameters

Parameter	Description	Value (pixels)	Physical Mapping
y_{top}	Y-pixel coordinate at top edge of plotting area	38	85 km altitude
y_{bottom}	Y-pixel coordinate at bottom edge of plotting area	586	45 km altitude
x_{left}	X-pixel coordinate at left edge of plotting area	59	-0.7 Hz frequency
x_{right}	X-pixel coordinate at right edge of plotting area	714	0.7 Hz frequency

Using the values from Table 2, altitude resolution (r_{alt}) and frequency resolution (r_{freq}) can be calculated as follows:



$$185 \quad r_{\text{alt}} = \frac{85 - 45}{y_{\text{bottom}} - y_{\text{top}}} = \frac{40 \text{ km}}{548 \text{ pixels}} \approx 0.073 \text{ km/pixel} \quad (4)$$

$$r_{\text{freq}} = \frac{0.7 - (-0.7)}{x_{\text{right}} - x_{\text{left}}} = \frac{1.4 \text{ Hz}}{655 \text{ pixels}} \approx 0.0021 \text{ Hz/pixel} \quad (5)$$

Given the bounding box $\mathbf{X} = [x_{\text{min}}, y_{\text{min}}, x_{\text{max}}, y_{\text{max}}]$ predicted by the model for a detected LIME, where $(x_{\text{min}}, y_{\text{min}})$ and $(x_{\text{max}}, y_{\text{max}})$ represent the top-left and bottom-right pixel coordinates respectively. Physical parameters were then calculated as:

$$190 \quad h_{\text{min}} = 85 - (y_{\text{max}} - y_{\text{top}}) \times r_{\text{alt}} \quad (6)$$

$$h_{\text{max}} = 85 - (y_{\text{min}} - y_{\text{top}}) \times r_{\text{alt}} \quad (7)$$

$$f_{\text{min}} = -0.7 + (x_{\text{min}} - x_{\text{left}}) \times r_{\text{freq}} \quad (8)$$

$$f_{\text{max}} = -0.7 + (x_{\text{max}} - x_{\text{left}}) \times r_{\text{freq}} \quad (9)$$

where h_{min} and h_{max} represent the minimum and maximum altitudes in Km, and f_{min} and f_{max} represent the minimum and maximum frequencies in Hz.

The script generated structured output datasets containing temporal data (date and time, extracted from filename), source information (folder, filename), and measured physical parameters for each processed spectrum. The results were systematically stored in an Excel file which allowed subsequent statistical analysis.

4 Results

200 4.1 Model performance

Model performance was evaluated on the validation set consisting of 40 annotated radar spectra. Core performance metrics are presented in Table3.

Table 3. Performance metrics overview

Core metrics	Value
Precision	89.1%
Recall	80.4%
mAP50	89.4%
F1	84.5%



The trained model achieved 89.4% mAP50, with precision (89.1%) notably higher than recall (80.4%). The higher precision compared to recall indicates fewer false positives than false negatives. The overall F1 score of 84.5% demonstrates robust
205 detection performance.

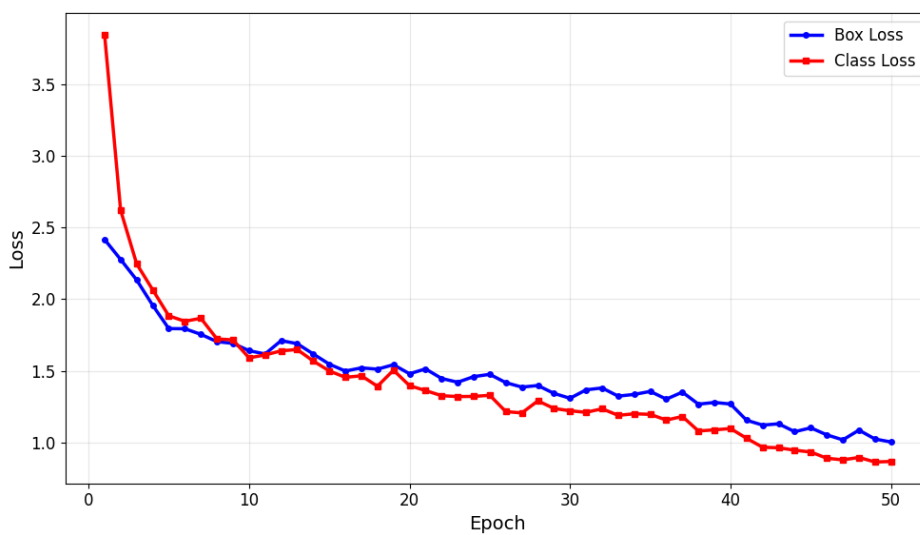


Figure 5. Training loss curves.

Yolov8 training optimises two loss components: box loss for bounding box localisation and classification loss for distinguishing between 'Target Signal' and 'Void' classes. Training losses over 50 epochs are illustrated in Fig. 5, showing both box and classification loss. Both losses exhibited rapid initial decrease during the first 10 epochs, followed by steady convergence. Training stabilised after approximately 30 epochs. The consistent downward trend without significant oscillation demonstrates
210 effective model optimisation.

Figure 6 illustrates the mAP50 evolution during training. The mAP50 exhibited rapid improvement during the initial 15 epochs, increasing from approximately 0.18 to 0.80. Performance continued to improve gradually, stabilising around 0.85 - 0.90 after epoch 20.

An example detection result is shown in Fig. 7. The figure shows the output of the trained model with two bounding boxes
215 which indicate the accurate identification and localisation of the 'Target_Signal' and 'Void' classes with confidence scores of 0.88 and 0.51, respectively. Thus, the model correctly identifies LIME with sufficient separation from D region echoes.

4.2 LIME characteristics

Physical parameters (altitude and frequency bounds) were extracted from each detection following the methodology described in Section 3.6. The mean altitude for each detection is calculated as the average of the minimum and maximum altitude bounds
220 of the bounding box. Similarly, spectral width is the difference between maximum and minimum frequency bounds. The automated pipeline processed radar spectra across four years (2018-2020 and 2024), identifying 12,677 LIME signatures that

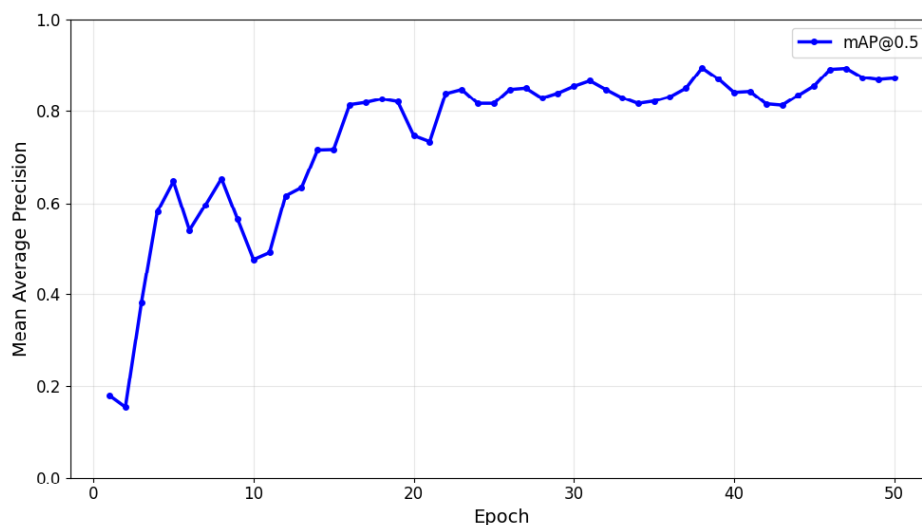


Figure 6. Evolution of mean Average Precision (mAP) at IoU threshold 0.5.

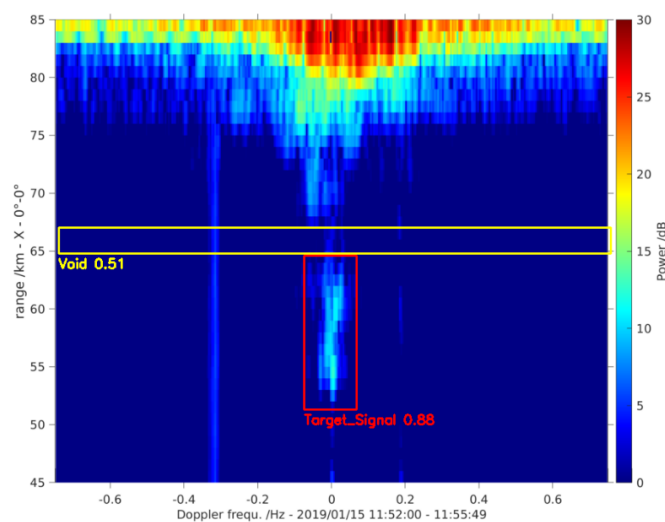


Figure 7. YOLOv8 detection results showing 'Target_Signal' identification and 'Void' region detection.

satisfied the two-class validation criterion. The following subsections present statistical analysis of the extracted parameters from the detected LIME.

4.2.1 Mean Altitude distribution

225 The composite mean altitude distribution from 12,677 valid detections across 2018-2020 and 2024 is shown in Fig. 8. The distribution exhibited a primarily Gaussian profile with mean altitude of 58.8 km and median of 58.5 km, indicating the pre-

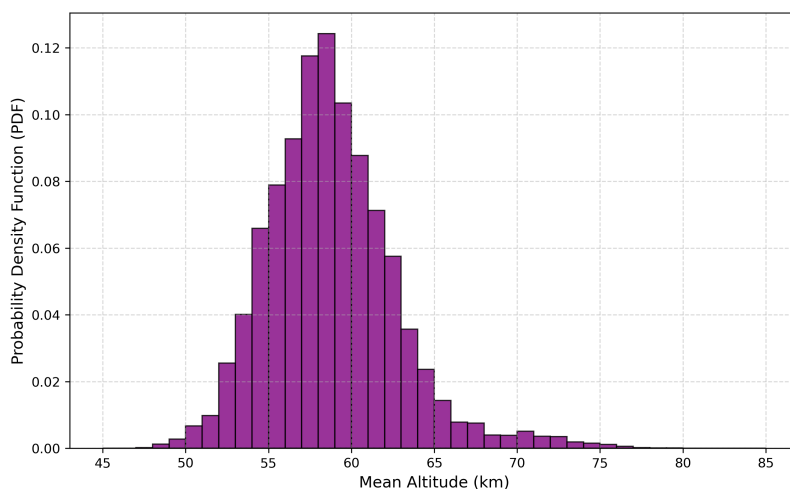


Figure 8. Composite probability density function of mean altitudes from years 2018-2020 and 2024 (12,677 total valid detections).

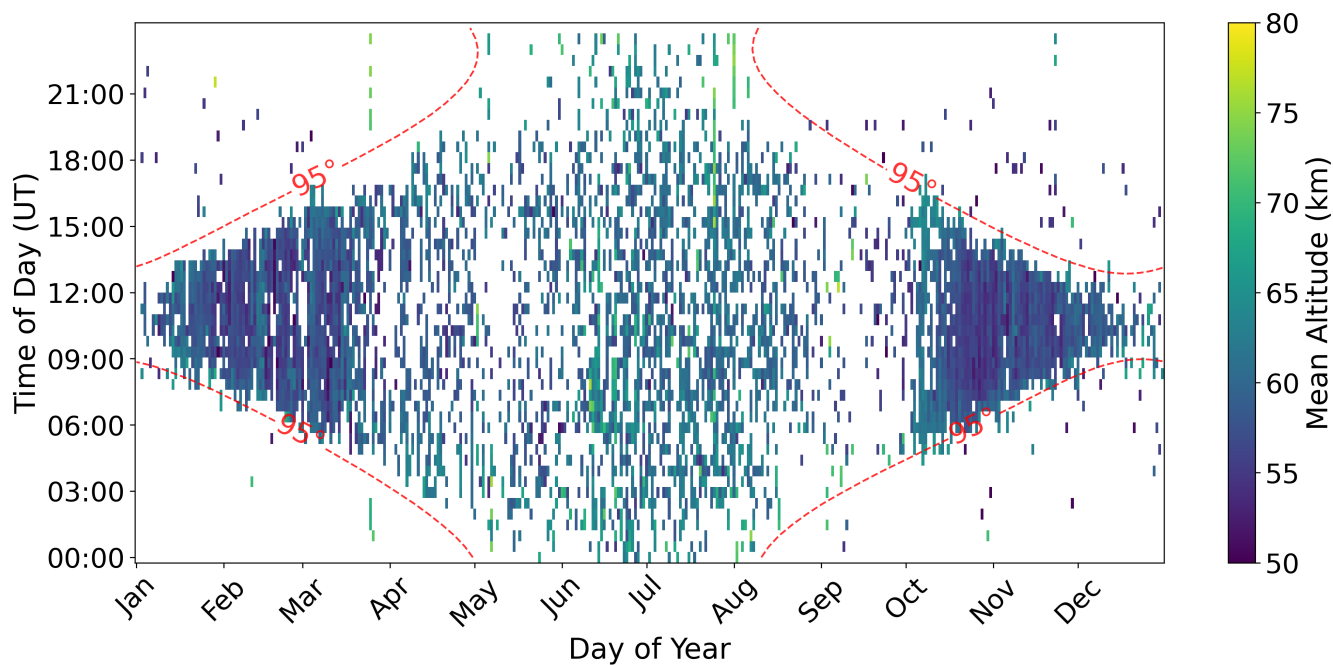


Figure 9. Temporal-altitude heatmap of LIME detections from years 2018-2020 and 2024. Data binned by day of year and 30-minute time intervals, with colors representing mean altitude averaged across all years.

dominant occurrence of LIME just below 60 km altitude. The detections above 70 km appear to be outliers possibly caused by interference. Figure 9 shows the composite temporal-altitude heatmap of LIME detections from all observational years as a function of day of year and time of day, with colors indicating the detected mean altitude. The red dashed contour marks



230 the solar zenith angle of 95° , representing the approximate boundary of daylight conditions. The vast majority of detections occurred when the solar zenith angle remained below 95° , indicating the necessity of solar illumination. A seasonal variation in the altitude can be observed, with LIME appearing at a higher altitude during summer months compared to winter months. For the majority of LIME cases we found a thickness of 6 to 10 km, whereas the larger number origins from events formed by two adjacent layers.

235 4.2.2 Spectral width analysis

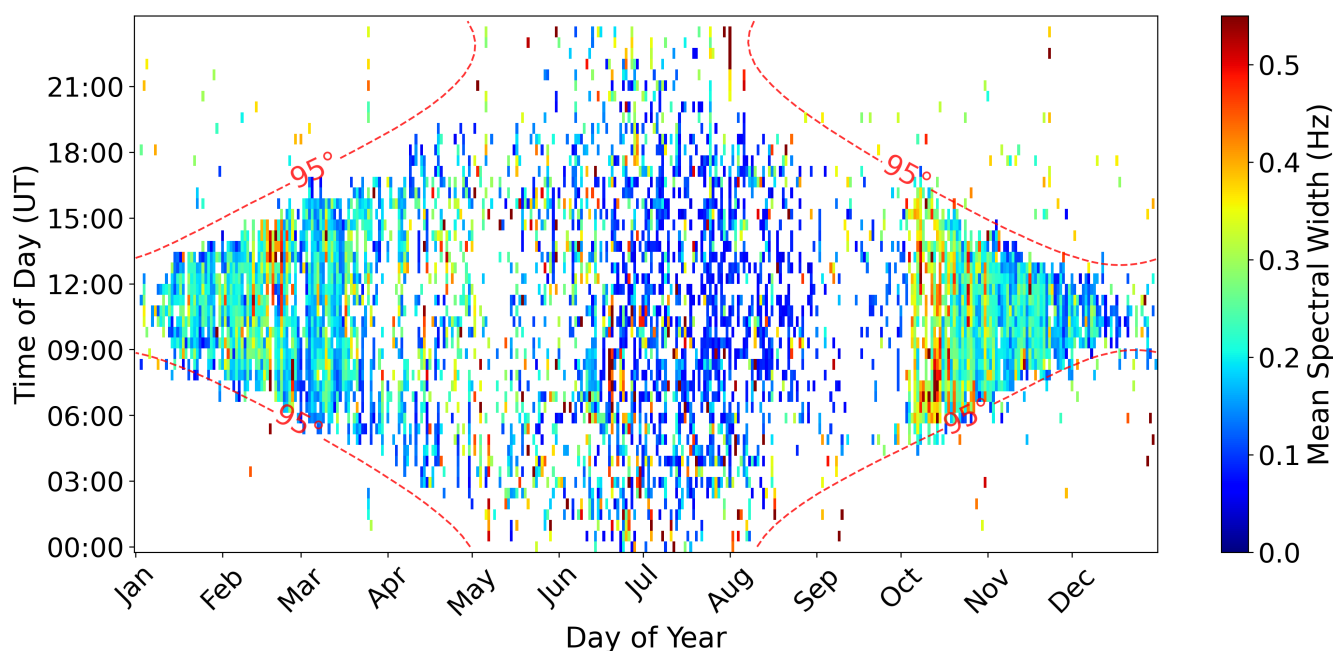


Figure 10. Temporal-spectral width heatmap of LIME detections from years 2018-2020 and 2024. Data binned by day of year and 30-minute time intervals, with colors representing mean spectral width averaged across all years.

Figure 10 shows the composite temporal-spectral width heatmap of LIME detections from all observational years as a function of day of year and time of day, with colors indicating mean spectral width. The heatmap indicates substantial variability in the spectral width of the LIME throughout the year. Seasonal variation was evident with October-March detections showing broader spectral widths (median = 0.21 Hz) compared to April-September (median = 0.14 Hz), indicating approximately 50% seasonal increase.

240

4.2.3 Temporal patterns

Figure 11 displays the median number of detections per 30-minute time bin across weekly intervals, calculated from four years (2018-2020 and 2024). The heatmap indicates that LIME appear more frequently during the winter weeks than during

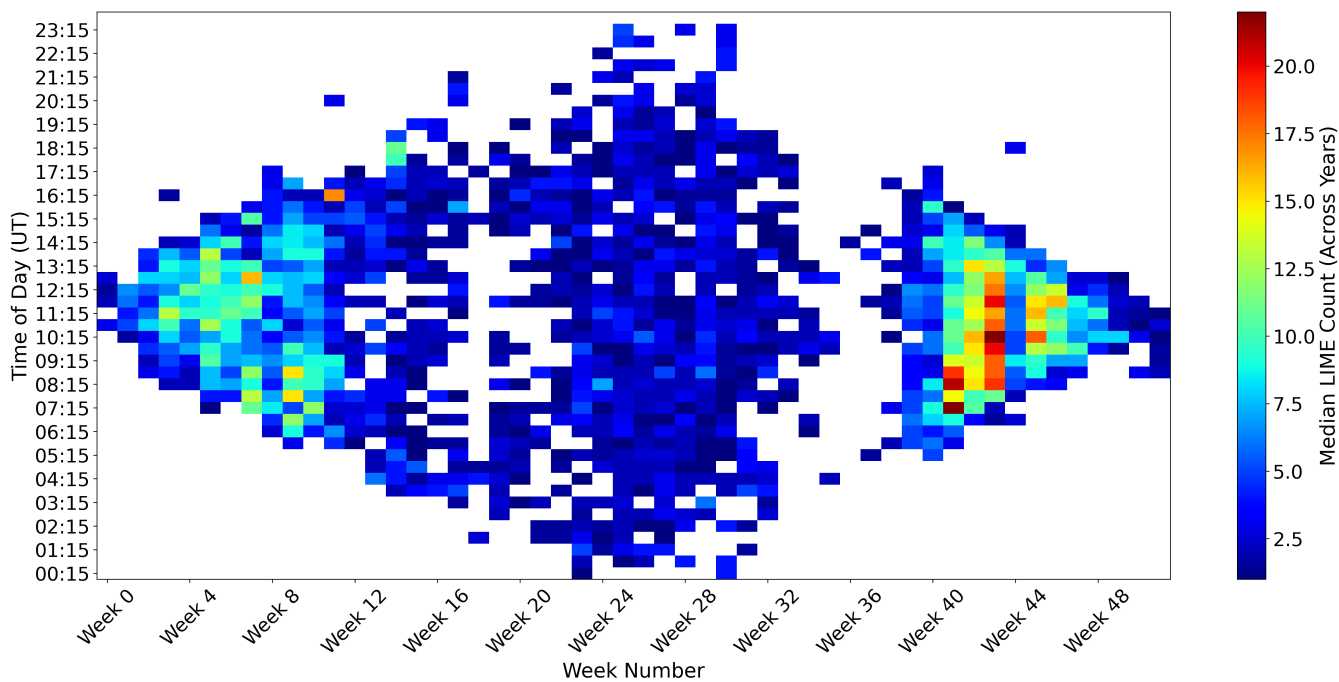


Figure 11. Weekly temporal distribution of median LIME occurrence from years 2018-2020 and 2024

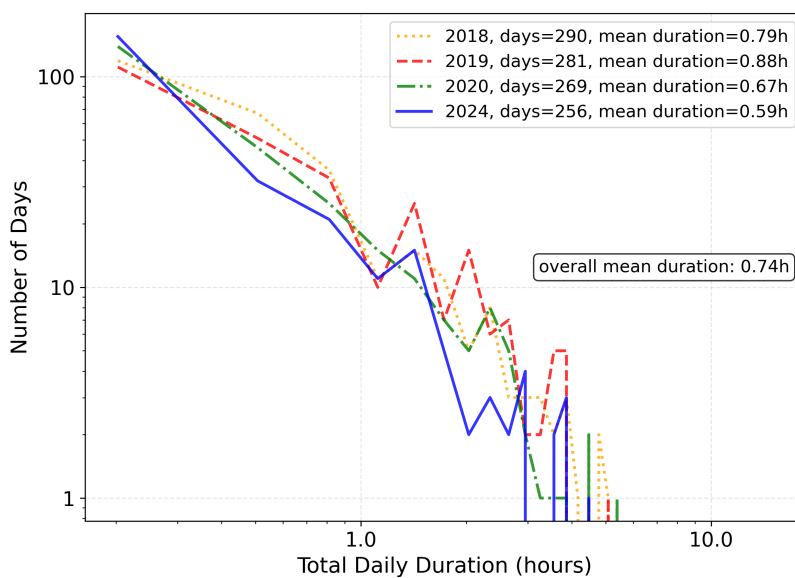
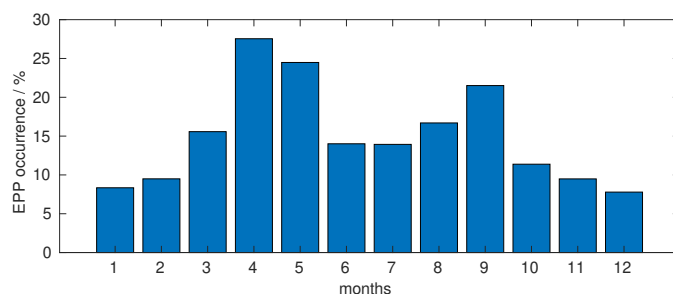


Figure 12. Daily LIME duration distributions from years 2018-2020 and 2024

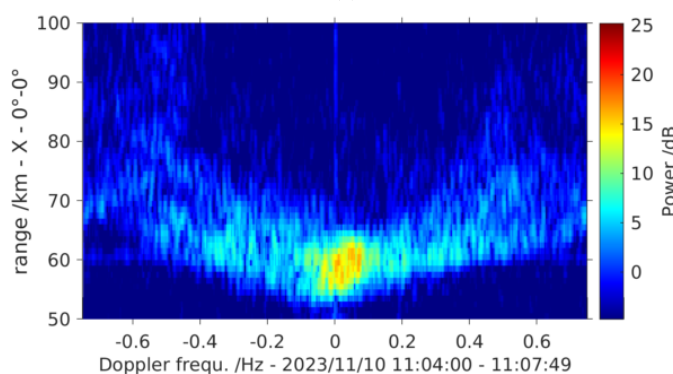


summer weeks. In summer, LIME were detected almost throughout the entire day due to low solar zenith angle (SZA), but overall occurrence count remained low compared to winter weeks. Figure 12 shows daily signal duration distribution for all observational years, calculated as the number of detections per day multiplied by the individual radar experiment duration. The distributions are plotted with both axes on logarithmic scales. The distribution exhibited exponential decay, with most days showing durations below 1 hour. Mean daily durations varied across years, ranging from 0.59 h (2024) to 0.88 h (2019), with an overall mean duration of 0.74 h.

250 5 Discussion



(a)



(b)

Figure 13. a) Monthly mean occurrence rate of EPP into the mesosphere, detected with Saura for the years 2003-2023. b) Image power spectrum of Saura for one experiment on Nov. 10 2023 displaying clear Doppler- and range-spread EPP signatures with a bottom altitude of about 56 km.

As we initially pointed out, radar echoes from an altitude of around 60 km are not uncommon at polar latitudes due to the presence of EPP; they can actually be observed for up to 40% of the time (Renkwitz and Latteck, 2017). However, these EPP-related radar echoes can be identified by their typical annual occurrence with a clear preference around the equinoxes as well as very distinct characteristics in the spectra of the radar time series. EPP events considerably enhance the ionization of

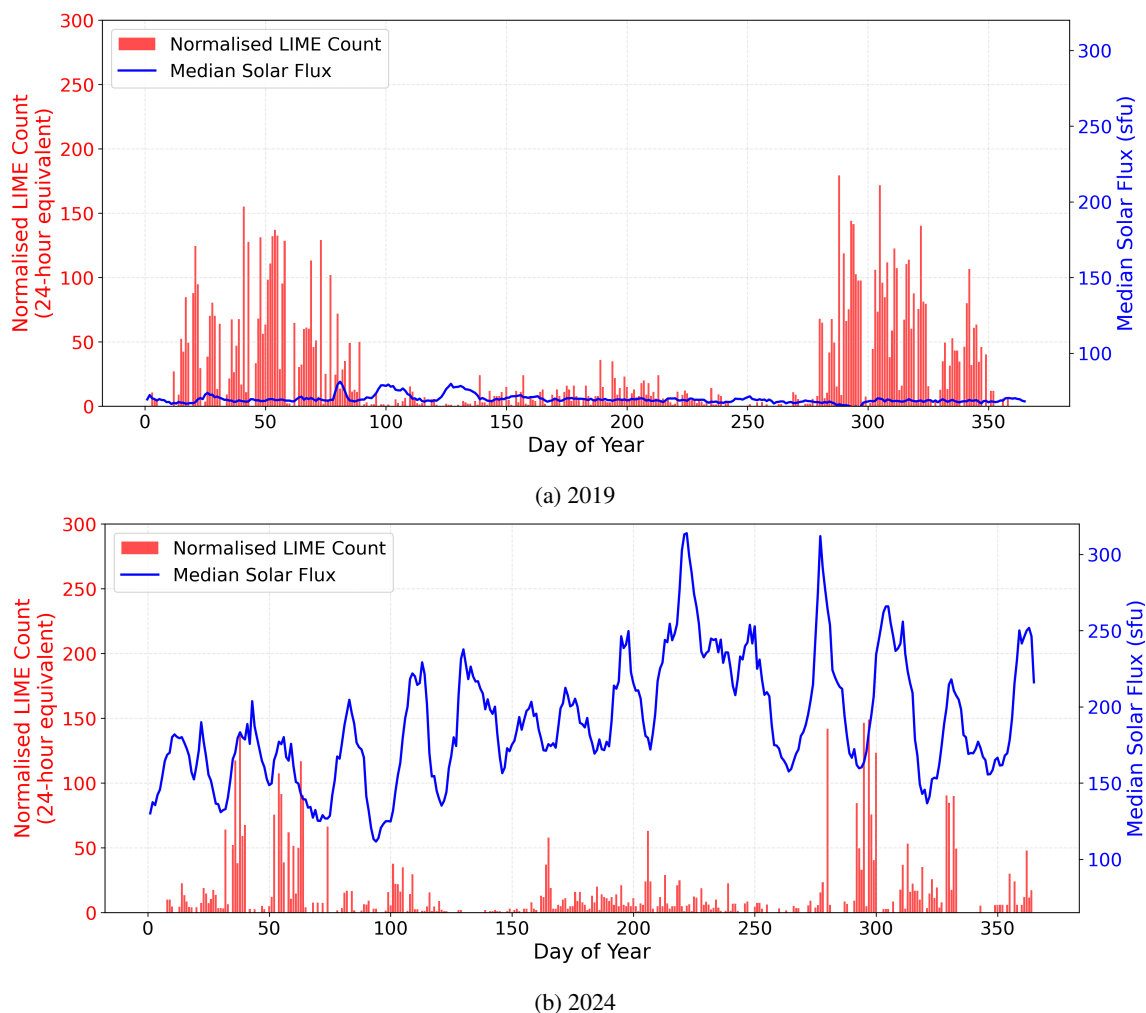


Figure 14. Normalised LIME counts vs. median solar flux for 2019 (top) and 2024 (bottom). Signal counts normalised by daylight hours ($SAZ \leq 95^\circ$)

255 the lower D region for areas with an extend of several dozens of km. While the quasi-simultaneous precipitation of similar
 energies occurs, and thus corresponding altitudes, pronounced parabolic arcs appear in the range intensity image spectra (see
 Fig. 13b). For the majority of such strong EPP, reaching 60 km altitude, the radar wave's energy is strongly absorbed during
 the propagation above that altitude, resulting in the absence of any radar echoes in the upper D and E or F region. In the case of
 LIME, no evidence of parabolic shaped signatures in the image spectra was found, nor it is clearly discernible in the statistics of
 260 the detection boxes spectral widths (see Fig. 10). Nevertheless there were situations when EPP echoes were observed at higher
 altitudes, e.g. near 70 km, and LIME occurred near 60 km, which however still did not show any EPP-like image spectrum.
 The LIMEs statistically have an obviously different occurrence distribution (Fig. 11) than EPP-related radar echoes (see Fig.



13a, similarly to Fig. 9 in Renkowitz and Latteck (2017), but extended to the end of 2023). LIME and EPP also show a clearly different altitude distribution. For LIME the winter season, October to March, seems to be preferred, which is possibly supported by the absence of the ordinary lower D region echoes as the solar zenith angle is too large. During summer, when the lesser solar zenith angle allows a lowered bottom side of the D region, LIME might be masked by the ordinary echoes. However, we still might expect to observe enhanced signatures of them at sun rise when the D region is yet not fully formed and equivalently for the sun set, which is not obvious in the shown statistics. At this point we may only speculate, that the generation mechanism allowing LIME is reduced during the summer months.

265 We also investigated a possible relation of the appearance of LIME to the solar activity. The normalized echo detections are depicted with the solar flux in Fig. 14a and Fig. 14b for the two years 2019 and 2024, which represent solar minimum and maximum conditions. EPP events are preferably seen during the ascending and descending phase of the solar maximum. Obviously LIME have been observed less frequently during solar maximum years. However, we can't identify a correlation between the occurrence and the solar flux for the investigated years ($r=-0.27$ and $r=-0.08$ for 2019 and 2024).

275 Interestingly, there are enhanced spectral widths visible for consecutive days in February and October for the four year average in Fig. 10. Spectral widening can be interpreted as enhanced turbulence, which might be caused by various dynamical situations like e.g. shear winds. However, the prominent intensification is quite remarkable and a possible source like changed tidal activity at these altitudes needs to be investigated.

Also, the detected altitudes seem to have preferred seasons (Fig. 9), where during October to March altitudes around 57 km are seen, whereas during summer higher altitudes are observed (≈ 61 km). This change of altitude occurs simultaneously with the reduction of spectral width and both could be an indicator for changes in the underlying driving mechanism of LIME.

The reduced occurrence of the echoes during summer is also visible in Fig. 12, where the long lasting echoes are comparably rare despite the long sunlit period during these months. Shorter durations up to one hour are much more frequent occurring during the short sunlit winter period.

285 Concerning possible false detections, we manually inspected some isolated detections that were associated to enhanced Doppler shift and spectral width. These short-lived detections are believed to originate from aircraft flying at a distance of about 55 km east of the radar, based on their appearance. These false detections were later suppressed by filtering the detected radar echoes Doppler shifts.

The detections outside the sunlit period are possibly caused by interference, but at most they only represent 1% of the total detections. We are therefore confident to have established a robust detection of LIME using YOLO.

295 A corresponding report about radar echoes that seemed to occur from below the D region was given by Rasmussen et al. (1980) using a bi-static ionospheric VLF/LF sounder. For the rather distant bi-static measurements they deduced the reflecting altitude at around 66 km with a thickness of 6 km and interpreted it as a layer of constant conductivity. Equivalent experiments in Brazil conducted in 1980 have shown similar results (Klemetti et al., 1988). Bain and Kossey (1987) addressed the initial publication by Rasmussen et al. (1980) and numerically found suitable altitudes near 63 km.

Even though the mentioned altitudes are near to what we report here, we doubt it's the same phenomenon as their plots show consistent echoes for consecutive days including the night times. Furthermore, the much lower frequency used in their



experiments means that also much less electron densities were required and one could also question the appropriate electron density profile they assumed for the reflection height calculations.

300 Another report on low altitude ionospheric echoes is given by Rietveld et al. (1996) using the EISCAT heater near 4 MHz frequency. For the conducted experiments around local noon signatures from below 60 km are prominent in their Fig. 7. Noteworthy, the electron density profile depicted in their Fig. 9 seems to resemble a rather enhanced ionisation state with $1e10$ electrons m^{-3} at 80 km altitude. Together with the comparably weak higher altitude D region echoes this scenario might rather be EPP related.

305 Later experiments by Vierinen et al. (2013) with the same heater conducted on 7 days in December 2011 for 1.5 h to 4 h duration during noontime have again shown radar echoes from 60 km altitude and partly below. During these days no significant geomagnetic distortion was found, nor did we see any EPP spectra in Saura radar data (130 km distant to the EISCAT heater). So, very likely no EPP occurred during these days that could have additionally ionized these low altitudes. Furthermore, in the shown examples no clear separation to the ordinary D region echoes to the 60 km echoes is visible, which might represent a
310 rather typical and consistent electron density profile.

Considering the amount of radiated power involved in these heating experiments, regular detection of echoes from as low as 60 km altitude with a radar frequency of 4 to 5 MHz seems plausible, but we're uncertain if it is connected to LIME we investigated in this manuscript.

As in most cases the observed LIME have a rather faint intensity, which indicates comparably small gradients in the radar
315 refractive index, which is defined by the electron density profile. Possible speculations for the appearance of LIME are:

- The present turbulence forms structures of favourable sizes in the refractive index under a nominal ionisation scenario. If so, why does this show altitude changes during sunrise and sunset whereas they prevail static most of the time in between at specific altitudes?
- Favourable conditions of mesospheric wind dynamics, resulting in a compression and accumulation of more neutrals
320 like nitric oxide that are then ionised by the same nominal ionization source?
- May changes of the incident ionisation source cause the visibility at preferred heights?

As one possible source galactic cosmic rays (GCR) may easily reach lower atmospheric altitudes and are measured on ground or on e.g. stratospheric balloons. GCRs are also believed to contribute as an ionisation source for the lowermost part of the D region. Interestingly GCRs should be reduced during enhanced solar activity and specifically during solar coronal mass
325 ejections (CME), which is called Forbush decrease (see e.g. Ross and Chaplin, 2019; Sierra-Porta, 2024; Riggi et al., 2025). From the last solar minimum to the current solar maximum GCR reductions of 30% and more have been observed. With the enhanced solar activity during 2024 and thus a reduction in GCR, we would also expect a reduced occurrence of LIME. This can actually be seen comparing Fig. 14a and 14b, which suggests GCR representing a significant ionisation source for the altitudes just below 60 km during solar minimum years.

330 Having discussed LIME characteristics from different perspectives like seasonal dependencies, solar flux correlations, and comparative analyses with the existing literature, let us now discuss the methodological framework used for this study. The



YOLOv8 object detection framework demonstrated robust transfer learning from natural images to atmospheric radar spectra images, achieving 89.4% mAP50 with only 200 annotated images. As noted in the Introduction, YOLO's demonstrated generalisation capability to specialised domains make it well-suited for the application to detect LIME, with recent studies confirming similar success across other remote sensing applications (Ma et al., 2025). The higher precision (89%) than recall (80.4%) reflects prioritisation of detection reliability over completeness. The automated detection approach processed one year of radar spectra in approximately 3 hours. This allowed systematic multi-year analysis that would have taken a substantially longer time with manual inspection. Future work could focus on improving the detection performance of the YOLOv8 model through improved annotation strategies and systematic hyperparameter tuning, potentially increasing the mAP50 beyond the current 89.4%.

6 Conclusions

In this study, we present the systematic analysis of radar echoes occurring from altitudes near 60 km, but are clearly separated from the regular D region. From this general appearance we named these radar echoes Low-altitude Isolated Mesospheric radar Echoes (LIME). These echoes were occasionally seen in typical radar range-time-intensity plots, but manual inspections for statistical analysis turned out to be very tedious and prone to human errors. Therefore the deep learning approach analysing about 350000 image power spectra of four years of radar observations revealed it as a still quite frequent phenomenon. The fine-tuned YOLOv8 model achieved 89.4% mAP50 with only 200 annotated spectra. So far we are not aware of any other report about LIME, which is likely reasoned by the uniqueness of the Saura radar in terms of its polar location, the radiated power and sensitivity at 3.17 MHz radar frequency.

The application of YOLO provided a robust and efficient way to detect and study these hardly described radar echoes from the lower mesosphere. New insights into the occurrence of LIME are derived from this analysis. The echoes are a daytime phenomenon, they exclusively occur during the sunlit period (99% for solar zenith angle $< 95^\circ$). The winter season (October to March) is the preferred period, during which the echoes partially show enhanced spectral widths for a few consecutive days. Whereas during summer, LIME seem to occur less frequently and with lesser spectral width. The preferred altitudes are near $57.5 \text{ km} \pm 4 \text{ km}$, whereas during summer the echoes are rather seen near 62 km. No clear numerical correlation between LIME and solar activity was found. However, we could clearly find a substantial decrease in LIME detections during the solar maximum year 2024. We relate this decrease to the expected reduction of GCR due to enhanced solar activity. Assuming this, GCR would demonstrate to play a significant role for ionisation processes just below 60 km altitude.

Continued observations and an extension of the analysis to more years of existing data will improve the statistics and by that might strengthen or actually clarify the speculated connection of GCR to the visibility of LIME. Furthermore, extending the investigations to multibeam data (off-vertical radar soundings) might indicate process properties like aspect-sensitivity or isotropy.



Data availability. The data to reproduce figures of the results are shared through radar-service.eu, the link will be shared with the editor/reviewers. A persistent DOI for public access to the data after acceptance is reserved.

365 *Author contributions.*

YK performed most of the analysis of the data, including the implementation and application of the YOLO based detection framework. TR had the main responsibility of the radar experiments, initially observed the radar echoes, did the first manual analysis, derived the image spectra and worked on the geophysical interpretation. AA helped with the concept, organisation and structuring of the work. All authors contributed to the writing of the article and preparation of figures. All authors have
370 read, corrected and agreed to the submitted version of the manuscript.

Competing interests.

The authors declare no conflict of interest.

Acknowledgements. The authors like to acknowledge discussions with Juha Vierinen from UiT, Mykhaylo Grygalashvyly and Jorge L. Chau from IAP. We acknowledge the use of Google Colaboratory for model training and computational resources. ChatGPT (OpenAI) was used
375 to refine wording in certain sections of this manuscript. After using this tool, the authors reviewed and revised as required and take full responsibility for the publication's content.



References

- Al Mudawi, N., Qureshi, A.M., Abdelhaq, M., Alshahrani, A., Alazeb, A., Alonazi, M., Algarni, A., 2023. Vehicle Detection and Classification via YOLOv8 and Deep Belief Network over Aerial Image Sequences. *Sustainability* 15, 14597. URL: <https://www.mdpi.com/2071-1050/15/19/14597>, doi:<https://doi.org/10.3390/su151914597>. publisher: Multidisciplinary Digital Publishing Institute.
- 380 Arabboev, M., Begmatov, S., Khamidjonov, Z., Aliyarov, X., Saydiakbarov, S., Vakhkhobov, S., Rikhsivoev, M., Nosirov, K., 2024. A comparative study of various object detection algorithms. *International Research Journal of Modernization in Engineering Technology and Science* 6, 2072–2079. doi:<https://doi.org/10.56726/IRJMETS59147>.
- Bain, W.C., Kossey, P.A., 1987. Characteristics of a reflecting layer below the classical D region. *Journal of Geophysical Research: Space Physics* 92, 12443–12444. doi:<https://doi.org/10.1029/JA092iA11p12443>.
- 385 Dev, S., Lee, Y.H., Winkler, S., 2017. Color-Based Segmentation of Sky/Cloud Images From Ground-Based Cameras. *IEEE Journal of Selected Topics in Applied Earth Observations and Remote Sensing* 10, 231–242. URL: <https://ieeexplore.ieee.org/document/7471439/>, doi:<https://doi.org/10.1109/JSTARS.2016.2558474>.
- Ferguson, M., Ak, R., Lee, Y.T.T., Law, K.H., 2018. Detection and Segmentation of Manufacturing Defects with Convolutional Neural Networks and Transfer Learning. *Smart and Sustainable Manufacturing Systems* 2, 137–164. URL: <https://dl.astm.org/ssms/article/2/1/137/17287/Detection-and-Segmentation-of-Manufacturing>, doi:<https://doi.org/10.1520/SSMS20180033>.
- 390 Friedrich, M., Pock, C., Torkar, K., 2017. Long-term trends in the d- and e-region based on rocket-borne measurements. *Journal of Atmospheric and Solar-Terrestrial Physics* 163, 78–84. doi:<https://doi.org/10.1016/j.jastp.2017.04.009>. long-term changes and trends in the upper atmosphere.
- 395 Galkin, I.A., Khmyrov, G.M., Kozlov, A., Reinisch, B.W., Huang, X., Kitrosser, D.F., 2006. Ionosonde networking, databasing, and web serving. *Radio Science* 41. doi:<https://doi.org/10.1029/2005RS003384>.
- Guo, B., Zhang, F., Li, W., Zhao, Z., 2024. Cloud Classification by Machine Learning for Geostationary Radiation Imager. *IEEE Transactions on Geoscience and Remote Sensing* 62, 1–14. URL: <https://ieeexplore.ieee.org/document/10400516/>, doi:<https://doi.org/10.1109/TGRS.2024.3353373>.
- 400 Klemetti, W.I., Kossey, P.A., Rasmussen, J.E., da Silverira Mecado Moura, M.S., 1988. VLF/LF Reflection Properties of the Low Latitude Ionosphere. *Environmental Research Papers Air Force Geophysics Laboratory, HANSCOM AFB, MA*.
- Ma, R., Yu, H., Liu, X., Yuan, X., Geng, T., Li, P., 2025. InSAR-YOLOv8 for wide-area landslide detection in InSAR measurements. *Scientific Reports* 15, 1595. URL: <https://www.nature.com/articles/s41598-024-84626-3>, doi:<https://doi.org/10.1038/s41598-024-84626-3>.
- 405 Oh, G., Lim, S., 2023. One-Stage Brake Light Status Detection Based on YOLOv8. *Sensors* 23, 7436. URL: <https://www.mdpi.com/1424-8220/23/17/7436>, doi:<https://doi.org/10.3390/s23177436>. publisher: Multidisciplinary Digital Publishing Institute.
- Rasmussen, J.E., Kossey, P.A., Lewis, E.A., 1980. Evidence of an Ionospheric Reflecting Layer below the Classical D Region. *Journal of Geophysical Research* 85, 3037 – 3044.
- Redmon, J., Divvala, S., Girshick, R., Farhadi, A., 2016. You Only Look Once: Unified, Real-Time Object Detection. URL: <http://arxiv.org/abs/1506.02640>, doi:<https://doi.org/10.48550/arXiv.1506.02640>. arXiv:1506.02640 [cs].
- 410 Reid, I.M., 2015. MF and HF radar techniques for investigating the dynamics and structure of the 50 to 110 km height region: a review. *Progress in Earth and Planetary Science* 2, 33. doi:<https://doi.org/10.1186/s40645-015-0060-7>.



- Renkowitz, T., Latteck, R., 2017. Variability of virtual layered phenomena in the mesosphere observed with medium frequency radars at 69°N. *Journal of Atmospheric and Solar-Terrestrial Physics* 163, 38 – 45. doi:<https://doi.org/10.1016/j.jastp.2017.05.009>.
- 415 Renkowitz, T., Sivakandan, M., Jaen, J., Singer, W., 2023. Ground-based noontime D-region electron density climatology over northern Norway. *Atmospheric Chemistry and Physics* 23, 10823–10834. doi:<https://doi.org/10.5194/acp-23-10823-2023>.
- Renkowitz, T., Tsutsumi, M., Laskar, F.I., Chau, J.L., Latteck, R., 2018. On the role of anisotropic MF/HF scattering in mesospheric wind estimation. *Earth, Planets and Space* 70, 158. doi:<https://doi.org/10.1186/s40623-018-0927-0>.
- Rietveld, M.T., Turunen, E., Matveinen, H., Goncharov, N.P., Pollari, P., 1996. Artificial periodic irregularities in the auroral ionosphere. *Annales Geophysicae* 14, 1437–1453. URL: <https://angeo.copernicus.org/articles/14/1437/1996/>, doi:<https://doi.org/10.1007/s00585-996-1437-0>.
- 420 Raggi, F., Hertle, L., Abbrescia, M., Avanzini, C., Baldini, L., Baldini Ferroli, R., Batignani, G., Battaglieri, M., Boi, S., Boike, J., Bossini, E., Carnesecchi, F., Cavazza, D., Cicalò, C., Cifarelli, L., Coccetti, F., Coccia, E., Corvaglia, A., De Gruttola, D., De Pasquale, S., Dietrich, P., Galante, L., Garbini, M., Gericke, E., Gnesi, I., Gramegna, F., Gramstad, E., Grazzi, S., Haland, E., Hatzifotiadou, D., La Rocca, P., Krebs, N., Landmark, S., Liu, Z., Mandaglio, G., Margotti, A., Maron, G., Maturilli, M., Mazziotta, M., Mulliri, A., Nania, R., Noferini, F., Nozzoli, F., Ould-Saada, F., Palmonari, F., Panareo, M., Panetta, M., Paoletti, R., Pellegrino, C., Perasso, L., Pinto, C., Pisano, S., Righini, G., Ripoli, C., Rizzi, M., Sartorelli, G., Scapparone, E., Schattan, P., Schioppa, M., Schrön, M., Scioli, G., Scribano, A., Selvi, M., Taiuti, M., Terreni, G., Trifirò, A., Trimarchi, M., Vistoli, C., Votano, L., Williams, M., Zacharias, S., Zichichi, A., Zuyewski, R., Pinazza, O., 2025. High latitude observation of the Forbush decrease during the May 2024 solar storms with muon and neutron detectors on Svalbard. *Advances in Space Research* 76, 1225–1239. doi:<https://doi.org/10.1016/j.asr.2025.05.023>.
- 430 Ross, E., Chaplin, W.J., 2019. The Behaviour of Galactic Cosmic-Ray Intensity During Solar Activity Cycle 24. *Solar Physics* 294, 8. doi:<https://doi.org/10.1007/s11207-019-1397-7>.
- Sampurno, R.M., Liu, Z., Abeyrathna, R.M.R.D., Ahamed, T., 2024. Intrarow Uncut Weed Detection Using You-Only-Look-Once Instance Segmentation for Orchard Plantations. *Sensors* 24, 893. URL: <https://www.mdpi.com/1424-8220/24/3/893>, doi:<https://doi.org/10.3390/s24030893>.
- 435 Sierra-Porta, D., 2024. A multifractal approach to understanding Forbush Decrease events: Correlations with geomagnetic storms and space weather phenomena. *Chaos, Solitons Fractals* 185, 115089. doi:<https://doi.org/https://doi.org/10.1016/j.chaos.2024.115089>.
- Singer, W., Latteck, R., Holdsworth, D.A., 2008. A new narrow beam Doppler radar at 3 MHz for studies of the high-latitude middle atmosphere. *Advances in Space Research* 41, 1488–1494. doi:<https://doi.org/10.1016/j.asr.2007.10.006>.
- 440 Siskind, D.E., Zawdie, K.A., Sassi, F., Drob, D.P., Friedrich, M., 2018. An Intercomparison of VLF and Sounding Rocket Techniques for Measuring the Daytime D Region Ionosphere: Theoretical Implications. *Journal of Geophysical Research: Space Physics* 123, 8688–8697. doi:<https://doi.org/10.1029/2018JA025807>.
- Situ, Z., Teng, S., Feng, W., Zhong, Q., Chen, G., Su, J., Zhou, Q., 2023. A transfer learning-based YOLO network for sewer defect detection in comparison to classic object detection methods. *Developments in the Built Environment* 15, 100191. URL: <https://linkinghub.elsevier.com/retrieve/pii/S266616592300073X>, doi:<https://doi.org/10.1016/j.dibe.2023.100191>.
- 445 Sivakandan, M., Peters, D.H.W., Mielich, J., Renkowitz, T., Latteck, R., Chau, J.L., 2025. Comparison of Interannual Oscillations in the F, E, and D-Region Ionosphere Using Longterm Ground-Based Measurements. *Journal of Geophysical Research: Space Physics* 130. doi:<https://doi.org/10.1029/2024JA033604>.
- Ultralytics, 2023. Ultralytics YOLOv8. <https://github.com/ultralytics/ultralytics>. Version 8.0.

<https://doi.org/10.5194/egusphere-2026-1030>

Preprint. Discussion started: 6 March 2026

© Author(s) 2026. CC BY 4.0 License.



- 450 Vierinen, J., Kero, A., Rietveld, M.T., 2013. High latitude artificial periodic irregularity observations with the upgraded EISCAT heating facility. *Journal of Atmospheric and Solar-Terrestrial Physics* 105-106, 253–261. doi:<https://doi.org/https://doi.org/10.1016/j.jastp.2013.08.012>.